Geophysical Journal International

Geophys. J. Int. (2022) **231,** 1031–1039 https://doi.org/10.1093/gji/ggac237
GJI Seismology

Theory of phase transmission fibre-optic deformation sensing

Andreas Fichtner [1], Adonis Bogris,[2] Thomas Nikas,[3] Daniel Bowden [1], Konstantinos Lentas [4], Nikolaos S. Melis,[4] Christos Simos,[5] Iraklis Simos[6] and Krystyna Smolinski[1]

[1] *Department of Earth Sciences, ETH Zurich, Switzerland. E-mail: andreas.fichtner@erdw.ethz.ch*
[2] *Department of Informatics and Computer Engineering, University of West Attica, Egaleo, Greece*
[3] *Department of Informatics and Telecommunications, National and Kapodistrian University of Athens, Athens, Greece*
[4] *National Observatory of Athens, Institute of Geodynamics, Greece*
[5] *Electronics and Photonics Laboratory, Department of Physics, University of Thessaly, Lamia, Greece*
[6] *Department of Electrical and Electronics Engineering, University of West Attica, Egaleo, Greece*

Accepted 2022 June 21. Received 2022 June 9; in original form 2022 March 25

SUMMARY

We present a theory and conceptual examples for fibre-optic deformation sensing based on phase changes of transmitted light. As a first result, we establish an exact relation between observable phase changes and the deformation tensor along the fibre. This relation is nonlinear and includes effects related to both local changes in fibre length and deformation-induced changes of the local refractive index. In cases where the norm of the deformation tensor is much smaller than 1, a useful first-order relation can be derived. It connects phase changes to an integral over in-line strain along the fibre times the local refractive index. When spatial variations of the refractive index are negligible, this permits the calculation of phase change measurements from distributed strain measurements, for instance, from distributed acoustic sensing (DAS). An alternative form of the first-order relation reveals that a directional sensitivity determines the ability of a point along the fibre to measure deformation. This directional sensitivity is proportional to fibre curvature and spatial variability of the refractive index. In a series of simple conceptual examples, we illustrate how a seismic wavefield is represented in a phase change time-series and what the role of higher-order effects may be. Specifically, we demonstrate that variable curvature along the fibre may lead to a multiplication of seismic waves, meaning that a single seismic wave appears multiple times in a recording of optical phase changes. Furthermore, we show that higher-order effects may be observable in specific scenarios, including deformation exactly perpendicular to the fibre orientation. Though higher-order effects may be realized in controlled laboratory settings, they are unlikely to occur in seismic experiments where fibre geometries are irregular and waves asymptotically propagate in all directions with all possible polarizations as a consequence of 3-D heterogeneity. Our results provide the mathematical foundation for the analysis of emerging transmission-based fibre-optic sensing data, and their later use in seismic event characterization and studies of Earth structure.

Key words: Computational seismology; Seismic instruments; Seismic tomography; Theoretical seismology; Wave propagation.

1 INTRODUCTION

Distributed acoustic sensing (DAS) is a family of technologies to measure deformation along a fibre-optic cable using interferometry of backscattered laser light (Hartog 2017). Following early applications in perimeter security or traffic and pipeline monitoring (e.g. Owen *et al.* 2012; Hill 2015), DAS became a widely used tool in seismic exploration and monitoring, where optical cables are often pre-installed in boreholes (e.g. Dean *et al.* 1996; Mateeva *et al.* 2013; Daley *et al.* 2013; Mateeva *et al.* 2014; Daley *et al.* 2014; Li *et al.* 2015; Daley *et al.* 2016; Hornmann 2016). The ability of DAS to record deformation in a broad frequency range from mHz to kHz with dense spatial sampling at metre scale (e.g. Lindsey *et al.* 2020; Paitz *et al.* 2021), makes it attractive also for seismological

applications. The possibility to piggy-back on existing fibre-optic telecommunication infrastructure has led to novel applications in urban seismology, with a focus on seismic hazard in densely populated areas, where large numbers of conventional seismic instruments may be difficult or expensive to deploy (e.g. Lindsey *et al.* 2017; Martin *et al.* 2017; Biondi *et al.* 2017; Ajo-Franklin *et al.* 2019; Spica *et al.* 2020; Yang *et al.* 2021). The relative ease of deploying fibre-optic cables in challenging terrain, enables seismological studies on glaciers (Walter *et al.* 2020; Klaasen *et al.* 2021), volcanoes (Klaasen *et al.* 2021; Currenti *et al.* 2021; Klaasen *et al.* 2022) and avalanche-prone slopes (Fichtner *et al.* 2021) that would not have been possible without DAS. In parallel, theoretical developments improved our understanding of how DAS data may be exploited, for instance, by ambient field interferometry (Paitz *et al.* 2019).

While backscattering allows DAS to achieve distributed measurements with an effective channel spacing in the centimetre range, it also limits the length of the fibre that can be interrogated, typically to a few tens of kilometres. Light intensity loss with increasing propagation distance along the fibre decreases the signal-to-noise ratio. Though emerging amplifier technologies may help to reduce this problem, the installation of amplifiers along existing telecommunication cables or in harsh terrain may not always be possible. Emerging alternative systems overcome this limitation by measuring deformation-induced changes in the phase (Marra *et al.* 2018; Bogris *et al.* 2021; Marra *et al.* 2022; Bogris *et al.* 2022; Bowden *et al.* 2022) or the polarization (Mecozzi *et al.* 2021) of transmitted laser light. The ability of transmission-based systems to achieve interrogation distances of hundreds or thousands of kilometres opens new opportunities to investigate seismic activity and Earth structure in remote regions where conventional seismic instrumentation is sparse, including, most importantly, the oceans and polar regions. The main drawback of transmission-based systems, however, lies in the averaging of deformation along the fibre. Phase or polarization changes are accumulated along the fibre, apparently erasing information about the location where the underlying deformation occurred. Hence, in contrast to DAS, the measurement is not distributed but integrated. As a consequence, it may be more challenging to use transmission measurements to infer Earth structure or earthquake locations.

Though few transmission-based sensing systems have recently become operational, it has not yet been investigated how exactly their measurements relate to deformation of the Earth or some other medium of interest. The primary intention of this work is to fill this gap.

In the following sections, we develop a theory for the calculation of observed optical phase changes caused by fibre deformation. Section 2 sets the general stage and leads to an approximation-free equation that relates the deformation field to phase change measurements. For typical seismic wavefields, where strain is much smaller than 1, this relation can be linearized, thereby producing various first-order approximations that can be found in Section 3. One of these approximations allows us to easily forward model phase change measurements and to synthesize them from DAS data, thereby enabling a comparison of the two measurement systems. Another approximation highlights the role of cable curvature, showing that the sensitivity of a fibre segment to deformation is proportional to the local curvature. The more a fibre is curved, the better it records deformation. Finally, in Section 4.2, we investigate under which conditions higher-order effects may be observable, coming to the conclusion that they can safely be ignored in most seismological applications.

2 GENERAL DEVELOPMENTS

We begin with the derivation of an exact relation between the deformation tensor $\mathbf{F}(\mathbf{x}, t)$ along the fibre and the traveltime $T(t)$ of a pulse that propagates from the beginning to the end of the fibre. The only assumption is that $T(t)$ is much smaller than the characteristic timescales of deformation, meaning that the fibre does not deform significantly while a pulse is propagating. To ease calculations, we adopt a parametrized representation of the fibre, with its position $\hat{\mathbf{x}}(s)$ given in terms of the arc length s. The latter ranges between 0 and the total length of the fibre L, as shown in Fig. 1.

2.1 Reference case of an undeformed fibre

Our starting point is the (hypothetical) reference case where the fibre is not deformed. The time it takes for a pulse to travel from fibre location $\hat{\mathbf{x}}(s)$ to the neighbouring location $\hat{\mathbf{x}}(s) + d\hat{\mathbf{x}}(s)$ is given by

$$dT = \frac{|d\hat{\mathbf{x}}(s)|}{c[\hat{\mathbf{x}}(s)]}\,, \tag{1}$$

where $c[\hat{\mathbf{x}}(s)]$ is the potentially space-dependent speed of light along the fibre. The coordinate $\hat{\mathbf{x}}$ is interpreted as a Lagrangian coordinate, meaning that it co-moves with the deforming fibre instead of being attached to the static reference frame. By definition of the arc length, we can express the total traveltime of the pulse through the fibre as

$$T = \int_{s=0}^{L} \frac{ds}{c[\hat{\mathbf{x}}(s)]}\,, \tag{2}$$

which is the integral over all differential traveltimes along the fiber.

2.2 Traveltimes under an arbitrary deformation field

Under deformation, position $\hat{\mathbf{x}}$ moves to a new position $\hat{\mathbf{x}} + \mathbf{u}(\hat{\mathbf{x}}, t)$, where $\mathbf{u}(\hat{\mathbf{x}}, t)$ is the displacement field, as illustrated in Fig. 1. To avoid clutter, we omit dependencies on s for the moment. The neighbouring point at the original position $\hat{\mathbf{x}} + d\hat{\mathbf{x}}$ moves to $\hat{\mathbf{x}} + d\hat{\mathbf{x}} + \mathbf{u}(\hat{\mathbf{x}} + d\hat{\mathbf{x}}, t)$. It follows that the traveltime of the pulse within the deformed segment of the cable is now

$$dT(t) = \frac{|d\hat{\mathbf{x}} + \mathbf{u}(\hat{\mathbf{x}} + d\hat{\mathbf{x}}, t) - \mathbf{u}(\hat{\mathbf{x}}, t)|}{c[\hat{\mathbf{x}}, \mathbf{u}(\hat{\mathbf{x}}, t)]}\,. \tag{3}$$

The denominator accounts for the fact that the speed of light may be a function of the deformation of the fibre. Since $d\hat{\mathbf{x}}$ is infinitesimally small, we can rewrite the numerator as

$$\mathbf{u}(\hat{\mathbf{x}} + d\hat{\mathbf{x}}, t) - \mathbf{u}(\hat{\mathbf{x}}, t) = \mathbf{F}(\hat{\mathbf{x}}, t)\, d\hat{\mathbf{x}}\,, \tag{4}$$

where the Cartesian components of the deformation tensor $\mathbf{F}$ are defined by

$$F_{ij} = \frac{\partial u_i}{\partial x_j}\,. \tag{5}$$

In terms of the deformation tensor, we can rewrite eq. (3) as

$$dT(t) = \frac{|d\hat{\mathbf{x}} + \mathbf{F}(\hat{\mathbf{x}}, t)\, d\hat{\mathbf{x}}|}{c[\hat{\mathbf{x}}, \mathbf{u}(\hat{\mathbf{x}}, t)]}\,, \tag{6}$$

which can be further simplified using the arc-length parametrization of the position vector $\mathbf{x}$. In fact, we find

$$d\hat{\mathbf{x}} = \frac{d\hat{\mathbf{x}}(s)}{ds}\, ds = \mathbf{e}(s)\, ds\,, \tag{7}$$

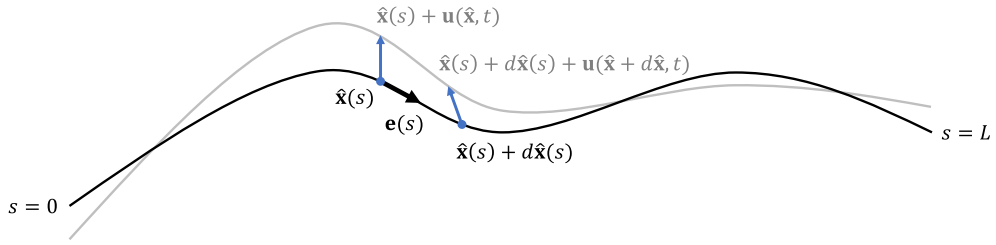

Figure 1. Schematic illustration of fibre deformation. The undeformed fibre, shown as black curve, is represented by the position vector $\hat{\mathbf{x}}(s)$, which is parametrized in terms of the arc length s. The cable starts at $s = 0$ and ends at $s = L$. Under a displacement field $\mathbf{u}(\hat{\mathbf{x}}, t)$, displayed as blue arrows, the Lagrangian position $\hat{\mathbf{x}}(s)$ along the undeformed fibre moves to $\hat{\mathbf{x}}(s) + d\hat{\mathbf{x}}(s)$. The result is the deformed fibre, shown in grey. The local tangent vector $\mathbf{e}(s)$ is shown as a thick black arrow.

where $\mathbf{e}(s)$ is the normalized tangent vector along the fibre. Thus, we obtain

$$dT(t) = \frac{|[\mathbf{I} + \mathbf{F}(\hat{\mathbf{x}}, t)]\,\mathbf{e}(s)|}{c[\hat{\mathbf{x}}, \mathbf{u}(\hat{\mathbf{x}}, t)]} ds\,, \tag{8}$$

and the total, time-dependent traveltime of the pulse becomes

$$T(t) = \int_{s=0}^{L} \frac{|[\mathbf{I} + \mathbf{F}(\hat{\mathbf{x}}, t)]\,\mathbf{e}(s)|}{c[\hat{\mathbf{x}}, \mathbf{u}(\hat{\mathbf{x}}, t)]} ds\,. \tag{9}$$

2.3 Phase changes in monochromatic signals

In the specific case of a monochromatic input with circular frequency ω, the traveltime difference $\Delta T(t) = T(t) - T$ translates into a phase difference

$$\phi(t) = \omega \Delta T(t)\,, \tag{10}$$

between the reference and the deformed state. Substituting eqs (2) and (9), we obtain

$$\phi(t) = \omega \int_{s=0}^{L} \frac{|[\mathbf{I} + \mathbf{F}(\hat{\mathbf{x}}, t)]\,\mathbf{e}(s)|}{c[\hat{\mathbf{x}}, \mathbf{u}(\hat{\mathbf{x}}, t)]} ds - \omega \int_{s=0}^{L} \frac{ds}{c[\hat{\mathbf{x}}(s)]}\,. \tag{11}$$

In the special case of no deformation, we have $\mathbf{u} = \mathbf{0}$ and $\mathbf{F} = \mathbf{0}$. Consequently, we obtain $|[\mathbf{I} + \mathbf{F}(\hat{\mathbf{x}}, t)]\,\mathbf{e}(s)| = |\mathbf{e}(s)| = 1$, and the phase difference ϕ vanishes, as required. Taking the time derivative of eq. (11), yields the phase changes $\partial_t \phi = \theta$ with respect to time,

$$\theta(t) = \omega \partial_t \int_{s=0}^{L} \frac{|[\mathbf{I} + \mathbf{F}(\hat{\mathbf{x}}, t)]\,\mathbf{e}(s)|}{c[\hat{\mathbf{x}}, \mathbf{u}(\hat{\mathbf{x}}, t)]} ds\,. \tag{12}$$

Eq. (12) is valid without any approximations, and it relates measured phase changes of the monochromatic laser signal to the displacement field $\mathbf{u}(\hat{\mathbf{x}}, t)$ along the fibre.

3 FIRST-ORDER APPROXIMATIONS

While being exact, eq. (12) is often too complicated to be practically useful. It can be simplified considerably by the standard continuum mechanics approach of excluding the seismic source region, that is, by limiting the analysis to those regions where the norm of the deformation tensor $\mathbf{F}$ is significantly smaller than 1. To avoid clumsy notation, we work with a slight reformulation of eq. (12), which uses the refractive index $r = c_0/c$, where c_0 is the speed of light in vacuum.

3.1 Relation to the strain tensor and DAS measurements

To obtain a first-order relation between phase changes and fibre deformation, we first note that

$$\begin{aligned} |[\mathbf{I} + \mathbf{F}]\,\mathbf{e}|^2 &= \mathbf{e}^T(\mathbf{F}^T + \mathbf{I}^T)(\mathbf{F} + \mathbf{I})\mathbf{e} \\ &= \mathbf{e}^T\mathbf{F}^T\mathbf{F}\mathbf{e} + \mathbf{e}^T\mathbf{F}^T\mathbf{e} + \mathbf{e}^T\mathbf{F}\mathbf{e} + \mathbf{e}^T\mathbf{e}\,. \end{aligned} \tag{13}$$

Neglecting the second-order term involving $\mathbf{F}^T\mathbf{F}$ and realizing that $\mathbf{e}^T\mathbf{e} = 1$ by definition of the unit tangent vector, we obtain

$$|[\mathbf{I} + \mathbf{F}]\,\mathbf{e}|^2 \doteq 1 + 2\mathbf{e}^T\mathbf{E}\mathbf{e}\,, \tag{14}$$

with the strain tensor $\mathbf{E} = (\mathbf{F}^T + \mathbf{F})/2$ and $\doteq$ meaning correct to first order in deformation quantities. Denoting the axial strain along the fibre as $\epsilon = \mathbf{e}^T\mathbf{E}\mathbf{e}$ and using the first-order relation $\sqrt{1 + 2\epsilon} \doteq 1 + \epsilon$, we arrive at

$$\theta(t) \doteq \frac{\omega}{c_0}\,\partial_t \int_{s=0}^{L} r[\hat{\mathbf{x}}, \mathbf{u}(\hat{\mathbf{x}}, t)]\;(1 + \epsilon[\hat{\mathbf{x}}(s), t])\;ds\,. \tag{15}$$

The dependence of the refractive index r on the deformation of the fibre is called the photoelastic effect, and it is primarily a dependence on the axial strain ϵ. Using the first-order Taylor approximation $r(\epsilon) \doteq r_0 + r'\epsilon$, we obtain the relation

$$\theta(t) \doteq \frac{\omega}{c_0}\,\partial_t \int_{s=0}^{L} r_{\text{eff}}[\hat{\mathbf{x}}(s)]\,\epsilon[\hat{\mathbf{x}}(s), t]\,ds\,, \tag{16}$$

where $r_{\text{eff}} = r_0 + r'$ is the effective refractive index, defined as the sum of the static refractive index r_0 and the axial strain derivative r', meaning that it takes the photoelastic effect into account. The derivative r' is commonly expressed in terms of the strain coefficient ξ as $r' = r_0(\xi - 1)$, with an experimentally determined value of $\xi \approx 0.78$ (Bertholds & Dändliker 1988). Eq. (16) provides a direct relation between phase changes θ measured by the transmission system, and the axial strain rate $\partial_t \epsilon$.

Eq. (16) is particularly interesting because it enables a direct and quantitative comparison of distributed strain measurements by DAS and integrated strain measurements by transmission-based systems such as the Microwave Frequency Fibre Interferometer (MFFI) of Bogris *et al.* (2021, 2022) or the ultrastable laser interferometer of Marra *et al.* (2018). In fact, when the effective refractive index is roughly constant along the fibre, it suffices to integrate DAS measurements of $\partial_t \epsilon$ along the fibre in order to synthesize transmission measurements of θ. Such a quantitative comparison of the MFFI system Bogris *et al.* (2021, 2022) and DAS can be found in Bowden *et al.* (2022).

3.2 Illustrative and educational examples

To understand the consequences of the first-order approximation (16), we continue with a series of simple examples. While they may not be realized exactly in practice, they still appear educationally valuable and insightful.

3.2.1 Deformation states

If a phase change is of first or second order in displacement $\mathbf{u}$ or deformation $\mathbf{F}$, depends on the geometry of fibre deformation. As a simple illustration, we consider the example in Fig. 2(a), where the displacement $\mathbf{u} = u_2\mathbf{e}_2$ is localized and perpendicular to the fibre direction $\mathbf{e}_1$. The length of the undeformed fibre is L, and the length of the deformed fibre is

$$L' = 2\sqrt{(L/2)^2 + u_2^2}\,. \tag{17}$$

Expanding L' into a Taylor series around $u_2 = 0$, yields

$$L' = L + \frac{2}{L}u_2^2 + \mathcal{O}(u_2^3)\,. \tag{18}$$

Eq. (18) implies that local deformation perpendicular to the fibre orientation is of second order in the displacement. Hence, there is no first-order effect on traveltimes and phase changes, and the second-order effect may be the only one observable, provided that u_2 is large enough to raise the observation above the noise level. An observable consequence of a dominant second-order effect is frequency doubling. To see this, we consider a harmonic deformation, $u_2 = \sin(2\pi ft)$, where f is frequency. Substituting u_2 into eq. (18), we find

$$L'(t) = L + \frac{1}{L}\left[1 - \cos(4\pi f t)\right] + \ldots\,, \tag{19}$$

It follows that the resulting length and phase changes oscillate with twice the frequency, $2f$, of the actual deformation.

We contrast the above example with a deformation style where the displacement is parallel to the fibre orientation, $\mathbf{u} = u_1\mathbf{e}_1$, as shown in Fig. 2(b). The length of the deformed fibre is

$$L' = L + u_1\,. \tag{20}$$

Hence, deformation along the fibre orientation has a first-order effect in $\mathbf{u}$ on length and phase changes. In the case of a harmonic deformation, the observed phase changes will have the same frequency as the deformation.

3.2.2 Fibre geometry

When second-order effects and changes in the refractive index throughout the fibre can be ignored, we merely need to solve the integral

$$I = \int_{s=0}^{L} \epsilon[\hat{\mathbf{x}}(s), t]\, ds\,, \tag{21}$$

to predict phase changes. To start simple, we let the fibre follow a straight line from $\hat{\mathbf{x}}(0) = \mathbf{0}$ to $\hat{\mathbf{x}}(L) = L\mathbf{e}_1$, where $\mathbf{e}_1$ is the unit vector in x_1-direction and therefore also the tangent vector $\mathbf{e}$. This fibre geometry is shown in Fig. 3(a). Evaluating eq. (21) gives

$$\begin{aligned} I &= \int_{s=0}^{L} \frac{\partial}{\partial x_1} u_1(s\mathbf{e}_1) ds = \int_{s=0}^{L} \frac{\partial}{\partial x_1} u_1(x_1\mathbf{e}_1) dx_1 \\ &= u_1(L\mathbf{e}_1) - u_1(\mathbf{0})\,. \end{aligned} \tag{22}$$

For a perfectly straight fibre, it follows that only the displacement at the beginning and the end of the fibre are measured, correct to first order. Hence, if the perturbation of interest is only present in between these two points, not affecting the beginning and end points, nothing can be measured.

In the second example, we again consider a fibre parallel to the $\mathbf{e}_1$ direction, which, however, returns to its starting point, as shown in Fig. 3(b). The parametrization of the fibre is now $\hat{\mathbf{x}}(s) = s\mathbf{e}_1$ for the first half, with s between 0 and $L/2$. For the second half, it is $\hat{\mathbf{x}}(s) = L\mathbf{e}_1 - s\mathbf{e}_1$, with s between $L/2$ and L. Using this to evaluate the integral (21), we find

$$I = 2u_1(L\mathbf{e}_1/2) - 2u_1(\mathbf{0})\,. \tag{23}$$

Hence, we again observe that only the start and the end point make a contribution to the measurement.

The fibre in our final example, shown in Fig. 3(c), features a 90° kink half way between the start and end points. The parametrization is $\hat{\mathbf{x}}(s) = s\mathbf{e}_1$ for s between 0 and $L/2$. For the second part, it is $\hat{\mathbf{s}} = L\mathbf{e}_1/2 + (s - L/2)\mathbf{e}_2$. Again evaluating the integral (21), yields

$$\begin{aligned} I = {} & u_1(L\mathbf{e}_1/2) - u_1(\mathbf{0}) + u_2(L\mathbf{e}_1/2 + L\mathbf{e}_2/2) \\ & - u_2(L\mathbf{e}_1/2)\,. \end{aligned} \tag{24}$$

Interestingly, in addition to the end points $\hat{\mathbf{x}}(0) = \mathbf{0}$ and $\hat{\mathbf{x}}(s) = L\mathbf{e}_1/2 + L\mathbf{e}_2/2$, also the kink point at $\hat{\mathbf{x}}(L/2) = L\mathbf{e}_1/2$ now makes a contribution, suggesting that curvature of the cable may play some role.

3.3 The role of fibre curvature and directional fibre sensitivity

To gain deeper understanding of these results, we go a few steps back and return to eq. (3). Denoting by $\hat{\mathbf{u}}(s,t) = \mathbf{u}[\hat{\mathbf{x}}(s), t]$ the displacement field along the fibre, we obtain

$$\begin{aligned} |d\hat{\mathbf{x}} + \mathbf{u}(\hat{\mathbf{x}} + d\hat{\mathbf{x}}, t) - \mathbf{u}(\hat{\mathbf{x}}, t)| &= |d\hat{\mathbf{x}} + \hat{\mathbf{u}}(s + ds, t) - \hat{\mathbf{u}}(s, t)| \\ &= |\mathbf{e}(s) + \partial_s \hat{\mathbf{u}}(s, t)|\, ds\,, \end{aligned} \tag{25}$$

where $\partial_s = \partial/\partial s$ denotes the derivative with respect to the arc length s. Using a similar development as in eqs (13) and (14), we may now obtain a first-order version of the approximation-free eq. (12). For this, we employ the first-order relation

$$|\mathbf{e}(s) + \partial_s \hat{\mathbf{u}}(s, t)| = 1 + \mathbf{e}(s)^T \partial_s \hat{\mathbf{u}}(s, t)\,, \tag{26}$$

and combine it with the Taylor expansion of the refractive index, $r(\epsilon) \doteq r_0 + r'\epsilon$. Recalling the definition $r_{\text{eff}} = r_0 + r'\epsilon$, then yields

$$\theta(t) \doteq \frac{\omega}{c_0}\, \partial_t \int_{s=0}^{L} \hat{r}_{\text{eff}}(s)\, \mathbf{e}(s)^T \partial_s \hat{\mathbf{u}}(s, t)\, ds\,, \tag{27}$$

where we defined, for convenience, $\hat{r}_{\text{eff}}(s) = r_{\text{eff}}[\hat{\mathbf{x}}(s)]$. Using the product rule,

$$\begin{aligned} \hat{r}_{\text{eff}}(s)\, \mathbf{e}(s)^T \partial_s \hat{\mathbf{u}}(s, t) = {} & \partial_s \left[\hat{r}_{\text{eff}}(s)\, \mathbf{e}(s)^T \hat{\mathbf{u}}(s, t)\right] \\ & - \partial_s \left[\hat{r}_{\text{eff}}(s)\, \mathbf{e}(s)^T\right] \hat{\mathbf{u}}(s, t)\,, \end{aligned} \tag{28}$$

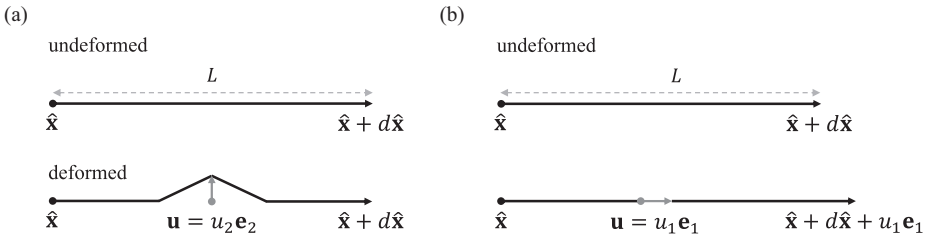

Figure 2. Simple examples of fibre deformation. (a) Deformation of an originally straight fibre perpendicular to its orientation, that is, by an amount u_2 in $\mathbf{e}_2$ direction. (b) Deformation of a straight fibre in the direction of its orientation, that is, by an amount u_1 in $\mathbf{e}_1$ direction.

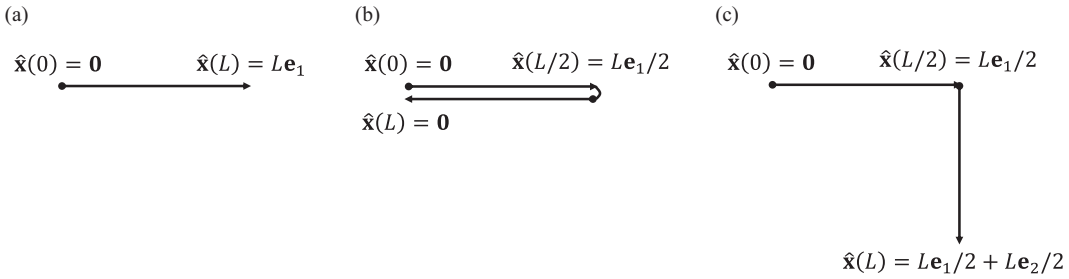

Figure 3. Simple examples of fibre geometries and corresponding arc length parametrizations.

and substituting back into eq. (16), we find

$$\theta(t) \doteq \underbrace{\frac{\omega}{c_0}\left[\hat{r}_{\text{eff}}(s)\,\mathbf{e}(s)^T\hat{\mathbf{v}}(s,t)\right]\Big|_{s=0}^{s=L}}_{\text{start/end point contribution}} - \underbrace{\frac{\omega}{c_0}\int_{s=0}^{L}\partial_s\left[\hat{r}_{\text{eff}}(s)\,\mathbf{e}(s)^T\right]\hat{\mathbf{v}}(s,t)\,ds}_{\text{curvature contribution}}, \tag{29}$$

with the displacement velocity $\hat{\mathbf{v}} = \partial_t\hat{\mathbf{u}}$. Eq. (29) has two contributions to the observed phase changes. The first one originates from the displacement at the start and end points of the fibre. It vanishes when the start and end points are not affected by deformation, which may happen in cases of rather localized deformation that only happens along a smaller section of the fibre or when the start and end points are mechanically isolated, for example, on an anti-vibration table.

The second contribution results from changes of the tangent vector and the refractive index along the fibre. In fact, the term

$$\mathbf{a}(s) = -\frac{\omega}{c_0}\,\partial_s\left[\hat{r}_{\text{eff}}(s)\,\mathbf{e}(s)\right] \tag{30}$$

plays the role of a directional fibre sensitivity. Assuming that deformation does not significantly affect the end points, we may use the directional sensitivity to rewrite eq. (29) as

$$\theta(t) \doteq \int_{s=0}^{L}\mathbf{a}(s)^T\,\hat{\mathbf{v}}(s,t)\,ds\,. \tag{31}$$

The amplitude of the directional sensitivity is proportional to changes of the refractive index along the fibre and to changes of the tangent vector $\mathbf{e}$. The latter is equivalent to the fibre being curved. Hence, strongly curved fibre segments have an inherently larger sensitivity to deformation than segments that are nearly straight. The strongest phase change signals will result from waves with polarization parallel to the directional sensitivity of a certain segment. In contrast, waves with polarization perpendicular to the directional sensitivity cannot be recorded by the respective segment.

4 CONCEPTUAL NUMERICAL EXAMPLES

The following examples are intended to (1) provide intuition for the relation between fibre deformation and phase change measurements $\theta(t)$, and (2) to estimate the second-order contributions that are difficult to quantify analytically. All examples are conceptual in nature and simplified, leaving complexities such as attenuation, anisotropy, heterogeneous coupling and fibre heterogeneities to future studies with actual data and concrete fibre layouts. We make the plausible assumption that the effective refractive index $\hat{r}_{\text{eff}}(s)$ is constant over a seismic wavelength, that is, $\mathcal{O}(10)$ km in our examples, thereby allowing us to ignore its derivative. Not trying to mimic a specific acquisition system, we set $\omega\hat{r}_{\text{eff}}/c_0 = 1\ \text{m}^{-1}$ for simplicity. With this setting, we have

$$\frac{\omega}{c_0}\int_{s=0}^{L}\partial_s\left(\hat{r}_{\text{eff}}(s)\,\mathbf{e}(s)^T\right)\hat{\mathbf{v}}(s,t)\,dt = \int_{s=0}^{L}\mathbf{n}(s)^T\hat{\mathbf{v}}(s,t)\,ds\,, \tag{32}$$

where $\mathbf{n}(s)$ is the non-normalized normal vector $\frac{d}{ds}\mathbf{e}(s)$. To avoid any complications, the elastic medium for our calculations is unbounded, isotropic and perfectly elastic, with P velocity $\alpha = 8000\,\text{m s}^{-1}$, S velocity $\beta = 5000\,\text{m s}^{-1}$ and density $\rho = 3000\,\text{kg m}^{-3}$. Well-known analytical solutions for moment tensor and single force sources may be found, for example, in Aki & Richards (2002).

4.1 Phase change measurements and fibre curvature

The influence of fibre geometry on the phase change recording $\theta(t)$ is illustrated in Fig. 4, where a P and S wavefield deform a fibre in the form of a sine curve. The directional sensitivity is proportional to curvature. Therefore, it is largest at the extrema of the sine curve and zero at the zero-crossings. Each of the high-curvature segments produces a distinct P-type arrival P_i and a corresponding S-type arrival S_i in the phase change time series. In total, eight P- and S-type arrivals can be distinguished, corresponding to the eight high-curvature segments.

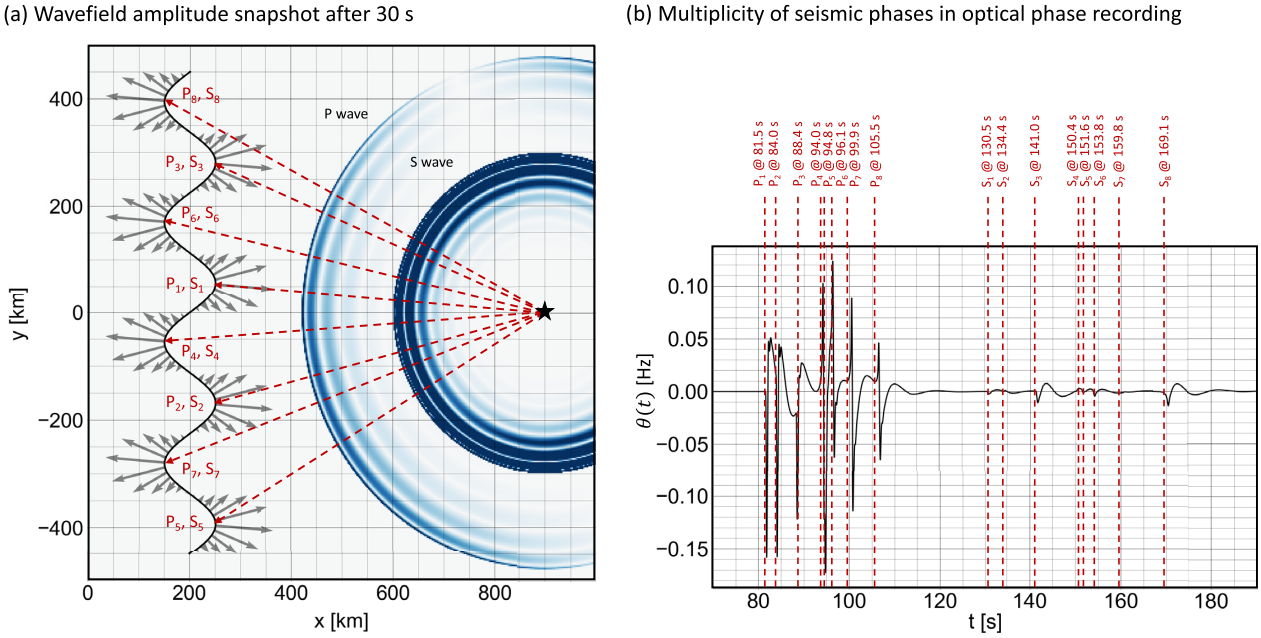

Figure 4. Example wavefield and phase change recording. (a) *P* and *S* wavefield originating from the source marked by the black star. The cable in the form of a sine curve is shown in black. Grey arrows are scaled versions of the directional sensitivity $\mathbf{a}(s)$. Its is parallel to the normal vector and has a length proportional to curvature. Red arrows point towards the cable segments with the largest curvature, which produce the highest-amplitude signals in the phase change recording. (b) The phase change recording consists of a sequence of pulses corresponding to the *P*- and *S*-wave arrivals at the high-curvature segments of the cable. These arrivals are labelled $P_{1,\,2,\ldots}$ and $S_{1,\,2,\ldots}$ in both panels.

Even though the *S*-wave amplitude is larger than the *P*-wave amplitude, the *S*-type arrivals in $\theta(t)$ are comparatively small. This effect is due to the *S*-wave polarization which, in contrast to the *P*-wave polarization, is nearly perpendicular to the directional sensitivity.

In summary, it follows that phase change measurements $\theta(t)$ may effectively produce a multiplet of seismic waves, which each singlet corresponding to a high-curvature segment of the cable and its wave path from the source. Generally, the amplitudes of the singlets are polarization-dependent and therefore not only related to the actual wave amplitude.

4.2 Estimation of second-order effects

In our next example, summarized in Fig. 5, we consider a single force acting in the *z*-direction. The cable, having the geometry of a circular segment in the *x*–*y*-plane, therefore only records the motion of an *S* wave, with polarization in *z*-direction. This scenario corresponds to the example from Fig. 2(a), where we deformed a fibre in the direction perpendicular to its orientation. There, we found, as a consequence of Pythagorean Theorem, that this style of deformation does not produce a first-order effect on the transmitted phase. Therefore, the higher-order effects may be visible. In fact, this is what we observe in Fig. 5(b). Using the exact, nonlinear forward modelling eq. (12), we obtain a phase change time-series that features an oscillation with frequencies much higher than the 0.1 Hz maximum frequency of the incoming wave. The signal starts to be visible at the time when the *S* wave reaches the point of the cable that is closest to the source. The amplitude of the signal then decays rapidly but remains at high frequency. Using the first-order approximation from eq. (29) does not reproduce this effect. Instead, as expected in the absence of any first-order effects, it produces a time-series that is identically zero for all times.

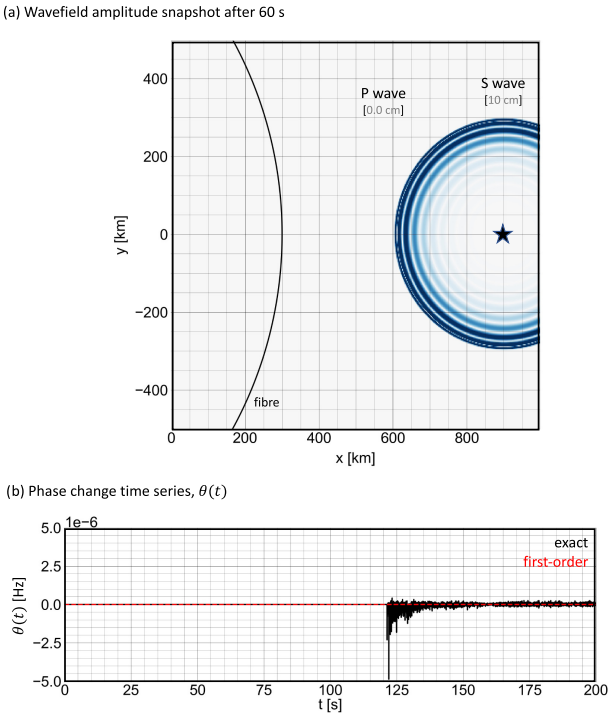

Figure 5. Exact solution versus first-order approximation. (a) Wavefield amplitude snapshot for a source that only produces an *S* wave within the *x*–*y*-plane where the fibre, shown as back curve, is located. The fibre has the shape of a circular segement with non-zero curvature, to ensure that the cable sensitivity is non-zero. The *P*-wave label with 0 cm amplitude is near the position where the *P*-wave front would be at that time, had it been excited. This pathological case is similar to the example in Fig. 2(a). The amplitude of the *S* wave (10 cm) is chosen to be unrealistically large in order to ensure that the second-order effect is not contaminated by floating-point errors. (b) Phase change time-series for the exact solution (black) and the first-order approximation (red).

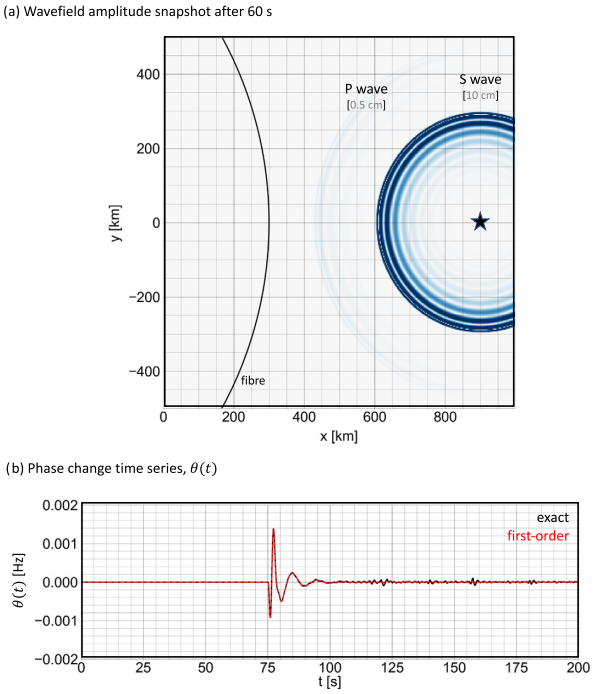

Figure 6. Exact solution versus first-order approximation. (a) Wavefield amplitude snapshot for a source that produces a small P wave (0.5 cm amplitude) and a large S wave (10 cm amplitude) within the x–y-plane where the fibre, shown as black curve, is located. Despite the unrealistically large amplitude of the S wave, which is responsible for the second-order effect, the first-order P-wave contribution dominates the phase change time-series in panel (b).

The calculation of higher-order effects can be a numerical challenge because they can be so small that floating point errors start to be important. This is also the case here, mostly because of the term $|(\mathbf{I}+\mathbf{F})\,\mathbf{e}|$, which requires us to compute the square root of a number that differs from 1 only by a number that is usually many orders of magnitude smaller than 1. To avoid this problem, the amplitude of the S wave in this example is unrealistically large, on the order of 10 cm. Such large displacements can only be observed near the epicentres of large earthquakes. Displacements in the micrometre range, would have been a more sensible choice from a seismological perspective.

In the next step, we slightly change the orientation of the single force source, to have a small component in x–y-direction, such that it produces a P wave recorded by the fibre in the x–y-plane, as shown in Fig. 6(a). Though the P wave has an amplitude that is around 20 times smaller than the amplitude of the S wave, it does produce a first-order effect that completely overwhelms the higher-order effects induced by the S wave, which are already unrealistically large. The agreement between the exact forward model (12) and the linear approximation (29) confirms the validity of the latter, even for displacement fields that are large compared to the majority of earthquake wavefields.

5 DISCUSSION

In the following, we provide additional discussion on simplifications and their range of validity, possible complications related to imperfect fibre coupling, the importance of higher-order effects and the possibility of mimicking a distributed sensing system.

5.1 Simplifications

The relation between observed optical phase changes θ and fibre deformation $\mathbf{F}$ is already complicated by the geometry of the fibre and the potential relevance of nonlinearity. While these mathematical complexities can be handled with reasonable effort and simplifications, there is also a range of practical issues that contribute to measurement errors in actual experiments, and that may be more challenging to control or quantify.

Often, the geometry of the fibre is only known to within metres or tens of metres. Fibre-optic cables deployed on glaciers or unstable slopes, for instance, may move considerably during the experiment. Telecommunication cables in particular may follow highly irregular paths that can only be estimated by coarse tap testing. The length and curvature of tightly wrapped cable segments, commonly used to provide some buffer that prevents tearing of the cable under long-term strain, may also not be well constrained, though they can make a significant contribution to the measurements, as shown in eq. (29).

A whole family of optical effects are likely to make an addition to the measurement errors., too. Optical fibres exhibit variations in the shape of their core along the fibre length, and they may experience non-uniform stress that breaks their cylindrical symmetry. The result is quasi-random and frequency-dependent birefringence that leads to polarization-mode dispersion (PMD) and an average differential group delay (DGD) $\Delta\tau$ between the two different polarization axes. For fibre lengths $\gg$1 km, DGD can be expressed as $\Delta\tau = D\sqrt{\ell}$, where D is the PMD coefficient and ℓ the length of the fibre segment (e.g. Agrawal 2012). For modern telecommunication fibres, D should be below 0.5 ps km$^{-1/2}$ (ITU 2022), thereby providing a quantitative measure of optical fibre heterogeneity that may be compared to the effect of fibre curvature on a case-by-case basis. Experimental research suggests that PMD at least plays a negligible role compared to the photoelastic effect (Butter & Hocker 1978).

5.2 Fibre coupling

A convenient but potentially profound simplification in our developments is the assumption that deformation of the medium, for example, the Earth, equals deformation of the fibre. Such perfect coupling is unlikely to be realized in practice, where the layout of fibre-optic cables must conform to the boundary conditions of a potentially harsh field site. Telecommunication cables, evidently, are not deployed for seismic experiments. Therefore, coupling may be somewhat random, and good coupling may to some extent be a matter of luck.

At least from a mathematical perspective, the effect of imperfect coupling can be incorporated easily into the theory presented above. For small deformation, the frequency-domain displacement velocity of the fibre, $\hat{\mathbf{v}}(s,f)$ and of the medium, $\hat{\mathbf{v}}_\oplus(s,f)$ are related by a linear coupling operator $\mathbf{C}(s,f)$ via $\hat{\mathbf{v}}(s,f) = \mathbf{C}(s,f)\,\hat{\mathbf{v}}_\oplus(s,f)$, where f is frequency. The resulting frequency-domain version of eq. (31) is

$$\theta(f) \doteq \int_{s=0}^{L} \mathbf{a}(s)^T\,\mathbf{C}(s,f)\,\hat{\mathbf{v}}_\oplus(s,f)\,ds\,. \tag{33}$$

Field experiments indicate that careful cable coupling, for example, by trenching and thermal insulation, may produce a coupling operator $\mathbf{C}(s,f)$ that is usefully independent of s and close to unity over a broad frequency range (Lindsey *et al.* 2020; Paitz *et al.* 2021), where the notion of useful is of course application-specific. Depending on the required measurement accuracy, calibration measurements to

estimate $\mathbf{C}(s, f)$ may be required, which could potentially defeat the purpose of fibre-optic measurements to not rely on installations of conventional point-localized sensors.

While it is certainly possible to reduce measurement errors by improving our knowledge of cable geometry, coupling and optical properties, an equally important effort is the design of suitable measurement functionals that honour the nature of the observational errors. During the past three decades, numerous measurement functionals have been developed for seismic inversion based on conventional seismometer recordings (e.g. Luo & Schuster 1991; Gee & Jordan 1992; Fichtner *et al.* 2008; Brossier *et al.* 2009; van Leeuwen & Mulder 2010; Bozdağ *et al.* 2011; Rickers *et al.* 2012). This effort may now need to be repeated for fibre-optic seismology.

5.3 Higher-order effects

As illustrated by eq. (12), a fibre-optic phase transmission system exhibits a nonlinear relation between the displacement field $\mathbf{u}$ and the observed output signal θ. The higher-order effects are characterized by higher frequencies, and they may be observable in cases where first-order effects are absent. This may be achieved in laboratory settings where the mode of deformation can be simple and controlled. However, in seismological applications it seems unlikely that first-order effects can be avoided, mainly for two reasons: (1) realistic fibre geometries are not perfect, meaning that some fibre segments are likely to be oriented such that the wavefield produces a first-order effect. (2) The seismic wavefield is complex, due to the 3-D heterogeneity and the presence of the Earth's surface with topography. Asymptotically, the seismic wavefield equipartitions, meaning that wave states with all possible propagation directions and polarizations will eventually occur, thereby producing some first-order effect.

Consequently, first-order effects will usually dominate the phase change observations by far. This means that linear forward modelling equations can be used, thereby facilitating the comparison to DAS data, as well as the calculation of sensitivity kernels with respect to Earth structure or source parameters.

5.4 Effective distributed sensing

The example in Section 4.1 illustrates that a single wave front may appear as a multiplet in a phase change recording. Each singlet corresponds to a segment of the fibre with high curvature, which the wave front reaches at different times. This suggests that a singlet is a measure of localized deformation near a strongly curved fibre segment that depends on Earth structure along the wave path between the source and the segment. In this sense, a curved fibre may mimic a distributed strain sensing system. An in-depth analysis of this effect can be found in a companion publication (Fichtner *et al.* 2022).

5.5 Earthquake location

An important corollary of our developments is that the cartoon-based suggestion of Marra *et al.* (2018) to locate earthquakes with phase-transmission fibre-optic measurements cannot be easily translated into practice. It operates under the incorrect assumption that the onset time of the phase change signal is generally produced by the fibre segment that is closest to the hypocentre. For example, in the extreme case of a perfectly straight segment there would be no measurement at all. Hence, earthquake location methods based on phase transmission still require more mathematical developments and a careful incorporation of the instrument response, which depends on the details of the fibre geometry.

6 CONCLUSIONS

We have developed a theory for deformation sensing using measurements of phase changes in transmitted laser pulses. Though the exact relation between deformation and phase change measurements is nonlinear, useful first-order approximations can be derived and justified for seismological applications where strain is typically much smaller than 1. The first of these relations connects phase changes to an integral of axial strain along the fibre, thereby enabling a direct comparison to measurements of distributed strain, for example, using DAS. The second relation establishes a link between the displacement field along the fibre and a directional fibre sensitivity. This sensitivity is proportional to spatial changes in refractive index and the curvature of the fibre. A possible consequence of spatially variable directional sensitivity is the multiple appearance of a single wave front in an optical phase change recording. Each singlet of the multiplet corresponds to a high-curvature segment of the fibre, thereby providing the opportunity to effectively mimic a distributed system with integrated strain sensing.

ACKNOWLEDGMENTS

The authors would like to thank the Editor-in-Chief Jörg Renner and an anonymous reviewer for their constructive comments. This work was partially funded by the Real-time Earthquake Risk Reduction for a Resilient Europe project (RISE) under the European Union's Horizon 2020 research and innovation programme (grant agreement no. 821115). Open-source code in the form of Python Jupyter Notebooks is available at https://github.com/afichtner/TransmissionFibreOptics.

REFERENCES

Agrawal, G.P., 2012. *Fiber-optic Communication Systems,* John Wiley & Sons.

Ajo-Franklin, J.B. *et al.*, 2019. Distributed acoustic sensing using dark fiber for near-surface characterisation and broadband seismic event detection, *Sci. Rep.,* **9,** doi:10.1038/s41598–018–36675–8.

Aki, K. & Richards, P., 2002. *Quantitative Seismology,* University Science Books.

Bertholds, A. & Dändliker, R., 1988. Determination of the individual strain-optic coefficients in single-mode optical fibers, *J. Lightwave Tech.,* **6,** 17–20.

Biondi, B., Martin, E., Cole, S., Karrenbach, M. & Lindsey, N., 2017. Earthquake analysis using data recorded by the Stanford DAS array, in *SEG Expanded Abstracts,* Vol. **2017,** pp. 2752–1756.

Bogris, A. *et al.*, 2021. *Microwave Frequency Dissemination Systems as Sensitive and Low-cost Interferometers for Earthquake Detection on Commercially Deployed Fiber Cables,* preprint (arXiv:2111.02957) [physics.geo-ph].

Bogris, A. *et al.*, 2022. *Sensitive Seismic Sensors based on Microwave Frequency Fiber Interferometers in Commercially Deployed Cables,* under review.

Bowden, D.C. *et al.*, 2022. *Linking Distributed and Integrated Fiber-optic Sensing,* preprint (arXiv:2205.11065).

Bozdağ, E., Trampert, J. & Tromp, J., 2011. Misfit functions for full waveform inversion based on instantaneous phase and envelope measurements, *Geophys. J. Int.,* **185,** 845–870.

Brossier, R., Operto, S. & Virieux, J., 2009. Robust elastic frequency-domain full waveform inversion using the l_1 norm, *Geophys. Res. Lett.,* **36,** L20310, doi:10.1029/2009GL039458.

Butter, C. & Hocker, G., 1978. Fiber optics strain gauge, *Appl. Opt.,* **17,** 2867–2869.

Currenti, G., Jousset, P., Napoli, R., Krawczyk, C. & Weber, M., 2021. On the comparison of strain measurements from fibre optics with a dense seismometer array at Etna volcano (Italy), *Solid Earth,* **12,** doi:10.5194/se–12–993–2021.

Daley, T.M., Pevzner, R., Shulakova, V., Kashikar, S., Miller, D.E., Goetz, J. & Lueth, J.H., 2013. Field testing of fiber-optic distributed acoustic sensing (DAS) for surbsurface seismic monitoring, *Leading Edge,* **June 2013,** 936–942.

Daley, T.M., White, D., Miller, D.E., Robertson, M., Freifeld, B., Herkenhoff, F. & Cocker, J., 2014. Simultaneous acquisition of distributed acoustic sensing VSP with multi-mode and single-mode optical cables and 3-component geophones at the Aquistore CO_2 storage site, *SEG Extended Abstract,* **2014,** 5014–5018.

Daley, T.M., Miller, D.E., Dodds, K., Cook, P. & Freifeld, B.M., 2016. Field testing of modular borehole monitoring with simultaneous distributed acoustic sensing and geophone vertical seismic profiles at Citronelle, Alabama, *Geophys. Prosp.,* **64,** 1318–1334.

Dean, T., Brice, T., Hartog, A., Kragh, E., Molteni, D. & O'Connell, K., 1996. Distributed vibration sensing for seismic acquisition, *Leading Edge,* **July 2016,** 600–604.

Fichtner, A., Kennett, B. L.N., Igel, H. & Bunge, H.-P., 2008. Theoretical background for continental- and global-scale full-waveform inversion in the time-frequency domain, *Geophys. J. Int.,* **175,** 665–685.

Fichtner, A. *et al.*, 2021. Observing avalanche dynamics with distributed acoustic sensing, in *EGU General Assembly 2021,* doi:10.5194/egusphere–egu21–16562.

Fichtner, A. *et al.*, 2022. *Sensitivity Kernels for Transmission Fiber Optics,* doi:10.48550/arXiv.2203.05229.

Gee, L.S. & Jordan, T.H., 1992. Generalized seismological data functionals, *Geophys. J. Int.,* **111,** 363–390.

Hartog, A., 2017. *An Introduction to Distributed Optical Fibre Sensors,* CRC Press, Boca Raton.

Hill, D., 2015. Distributed acoustic sensing (DAS): theory and applications, *Front. Opt.,* **2015,** doi:10.1364/FIO.2015.FTh4E.1.

Hornmann, J.C., 2016. Field trial of seismic recording using distributed acoustic sensing with broadside sensitive fibre-optic cables, *Geophys. Prosp.,* **65,** doi:10.1111/1365–2478.12358.

ITU, 2022. *ITU Recommendations,* https://www.itu.int/en/ITU-T/publications/Pages/recs.aspx.

Klaasen, S., Paitz, P., Lindner, N., Dettmer, J. & Fichtner, A., 2021. Distributed acoustic sensing in volcano-glacial environments—Mount Meager, British Columbia, *J. Geophys. Res.,* **159,** doi:10.1029/2021JB022358.

Klaasen, S., Thrastarson, S., Fichtner, A., Cubuk-Sabuncu, Y. & Jonsdottir, K., 2022. Sensing Iceland's most active volcano with a "buried hair", *EOS,* **103,** doi:10.1029/2022EO220007.

Li, M., Wang, H. & Tao, G., 2015. Current and future applications of distributed acoustic sensing as a new reservoir geophysics tool, *Open Petr. Eng. J.,* **8,** 272–281.

Lindsey, N.J., Martin, E.R., Dreger, D.S., Freifeld, B., Cole, S., James, S.R., Biondi, B.L. & Ajo-Franklin, J.B., 2017. Fiber-optic network observations of earthquake wavefields, *Geophys. Res. Lett.,* **44,** 11792–11799.

Lindsey, N.J., Rademacher, H. & Ajo-Franklin, J.B., 2020. On the broadband instrument response of fiber-optic DAS arrays, *J. geophys. Res.,* **125,** doi:10.1029/2019JB018145.

Luo, Y. & Schuster, G.T., 1991. Wave-equation traveltime inversion, *Geophysics,* **56,** 645–653.

Marra, G. *et al.*, 2018. Ultrastable laser interferometry for earthquake detection with terrestrial and submarine cables, *Science,* **361,** 486–490.

Marra, G. *et al.*, 2022. Optical interferometry-based array of seafloor environmental sensors using a transoceanic submarine cable, *Science,* **376,** 874–879.

Martin, E.R., Castillo, C.M., Cole, S., Sawasdee, P.S., Yuan, S., Clapp, R., Karrenbach, M. & Biondi, B.L., 2017. Seismic monitoring leveraging existing telecom infrastructure at the SDASA: Active, passive, and ambient-noise analysis, *Leading Edge,* **36,** 1025–1031.

Mateeva, A. *et al.*, 2013. Distributed acoustic sensing for reservoir monitoring with VSP, *Leading Edge,* **October 2013,** 1278–1283.

Mateeva, A. *et al.*, 2014. Distributed acoustic sensing for reservoir monitoring with vertical seismic profiling, *Geophys. Prosp.,* **62,** 679–692.

Mecozzi, A., Cantono, M., Castellanos, J.C., Kamalov, V., Muller, R. & Zhan, Z., 2021. Polarization sensing using submarine optical cables, *Optica,* **8,** doi:10.1364/OPTICA.424307.

Owen, A., Duckworth, G. & Worsley, J., 2012. Fibre-optic distributed acoustic sensing for border monitoring, in *2012 European Intelligence and Security Informatics Conference,* doi:10.1109/EISIC.2012.59.

Paitz, P., Sager, K. & Fichtner, A., 2019. Rotation and strain ambient noise interferometry, *Geophys. J. Int.,* **216,** 1938–1952.

Paitz, P., Edme, P., Gräff, D., Walter, F., Doetsch, J., Chalari, A., Schmelzbach, C. & Fichtner, A., 2021. Empirical investigations of the instrument response for distributed acoustic sensing (DAS) across 17 octaves, *Bull. seism. Soc. Am.,* **111,** 1–10.

Rickers, F., Fichtner, A. & Trampert, J., 2012. Imaging mantle plumes with instantaneous phase measurements of diffracted waves, *Geophys. J. Int.,* **190,** 650–664.

Spica, Z.J., Perton, M., Martin, E.R., Beroza, B.C. & Biondi, B., 2020. Urban seismic site characterization by fiber-optic seismology, *J. geophys. Res.,* **125,** doi:10.1029/2019JB018656.

van Leeuwen, T. & Mulder, W.A., 2010. A correlation-based misfit criterion for wave-equation traveltime tomography, *Geophys. J. Int.,* **182,** 1383–1394.

Walter, F., Gräff, D., Lindner, F., Paitz, P., Köpfli, M., Chmiel, M. & Fichtner, A., 2020. Distributed Acoustic Sensing of microseismic sources and wave propagation in glaciated terrain, *Nat. Comm.,* **11,** doi:10.1038/s41467–020–15824.

Yang, Y., Atterholt, J.W., Shen, Z., Muir, J.B., Williams, E.F. & Zhan, Z., 2021. Sub-kilometer correlation between near-surface structure and ground motion measured with distributed acoustic sensing, *Geophys. Res. Lett.,* **49**(1), doi:10.1029/2021GL096503.